

# Quantized Charge Accumulation in a Quantum Anomalous Hall System

Yuanze Li<sup>1</sup>, Jiahao Chen<sup>1</sup>, Renfei Wang<sup>2</sup>, Yifan Zhang<sup>3</sup>, Yingdong Deng<sup>4</sup>,  
Jin Xie<sup>4</sup>, Xufeng Kou<sup>3,5</sup>, Yang Liu<sup>2</sup>, Tian Liang<sup>1,6\*</sup>

<sup>1</sup>State Key Laboratory of Low Dimensional Quantum Physics, Department of Physics, Tsinghua University, Beijing 100084, People's Republic of China.

<sup>2</sup>International Center for Quantum Materials, Peking University, Beijing 100871, People's Republic of China.

<sup>3</sup>School of Information Science and Technology, ShanghaiTech University, Shanghai 201210, People's Republic of China.

<sup>4</sup>School of Physical Science and Technology, ShanghaiTech University, Shanghai 201210, People's Republic of China.

<sup>5</sup>ShanghaiTech Laboratory for Topological Physics, School of Physical Science and Technology, ShanghaiTech University, Shanghai 201210, People's Republic of China.

<sup>6</sup>Frontier Science Center for Quantum Information, Beijing 100084, People's Republic of China.

\*Corresponding author. E-mail: [tliang@mail.tsinghua.edu.cn](mailto:tliang@mail.tsinghua.edu.cn);

## Abstract

We report the first experimental observation of magnetic-field-induced quantized charge accumulation in a quantum anomalous Hall (QAH) system—a phenomenon originating from the intrinsic two-dimensional surface state and fundamentally distinct from conventional edge-dependent transport phenomena. Our approach employs a novel out-of-plane capacitive detection method to directly probe this charge accumulation, revealing its distinction and correlation with other surface state properties, such as Laughlin charge pumping. We demonstrate that the accumulated charge density is governed by the quantized Hall conductance but is significantly influenced by dissipation effects due to finite longitudinal conductance. By performing frequency and longitudinal conductance dependence measurements, the underlying ideal quantized charge accumulation is extracted, in agreement with theoretical predictions. Importantly, our out-of-plane method of measuring charge accumulation allows the detection of small electric polarization in future studies, establishing a pathway toward the direct observation of the topological magnetoelectric effect, a manifestation of the four-dimensional quantum Hall effect.

## 1 Introduction

The quantum anomalous Hall (QAH) effect represents a hallmark phenomenon in topological materials, attracting sustained attention since its theoretical prediction and first experimental realization [1–4]. The QAH system features a quantized Hall conductance and vanishing longitudinal conductance similar to the quantum Hall (QH) effect. However, the QAH effect requires no external magnetic field, as it arises from the intrinsic magnetization of the material. Magnetically ordered three-dimensional (3D) topological insulators (TIs) serve as the primary material platform for realizing the QAH effect [4–7],

where the top and bottom surfaces of a thin film sample each contribute a half-quantized Hall conductance,  $\sigma_{xy}^s = \pm e^2/2h$ , with the sign depending on the surface magnetization direction. When combined, both surfaces yield the integer-quantized Hall conductance  $\sigma_{xy} = \pm e^2/h$ . The half-quantization of the surface state originates from a massive Dirac Hamiltonian, which arises when the exchange interaction from surface ferromagnetism gaps the surface states of 3D TIs [8, 9]. The analysis based on Berry curvature yields  $\pm e^2/2h$  for each surface, establishing a topologically nontrivial surface state.

The remarkable signatures of the QAH effect—quantized Hall conductance and vanishing longitudinal conductance observed in Hall-bar experiments—are conventionally explained by the presence of a one-dimensional (1D) chiral edge state [8, 10]. The edge channel forms as a domain wall where the surface Hall conductance changes from  $+e^2/2h$  to  $-e^2/2h$ , yielding a chiral edge state at the physical boundary of the sample. However, this model oversimplifies a fundamentally two-dimensional (2D) effect into a boundary phenomenon. The QAH state originates from the quantized Hall conductance of the entire surface, in other words, it is intrinsically a 2D phenomenon. Consequently, although transport measurements in Hall-bar geometries are technically convenient and powerful for confirming quantization, they can only provide an indirect probe of the underlying 2D surface properties as the interpretation of the Hall signal in Hall-bar geometry is unnecessarily convoluted by the edge state. Therefore, developing experimental techniques that can directly access the intrinsic surface Hall conductance, independent of sample edges, is essential for a more complete understanding of the QAH effect.

To this end, a few experimental approaches have been developed. One prominent method is the optical Hall measurement based on time-domain terahertz spectroscopy (TDTS), which detects the Faraday and Kerr rotations as signatures of the surface Hall conductance, while avoiding contributions from edge channels by spatially isolating the beam spot from the sample boundary [11–14]. Another approach, inspired by Laughlin’s charge pumping model [15], measures the quantized adiabatic charge transfer between the inner and outer contacts of a Corbino disk sample under field variation [16, 17], yielding quantized Hall conductance  $\sigma_{xy}$ . In the Corbino disk geometry, the charge pumping proceeds entirely through the adiabatic variation of 2D states, eliminating the involvement of edge channels.

Different from previous methods, here we propose for the first time a conceptually distinct approach of directly detecting the quantized charge accumulation induced by magnetic field variations on the quantum Hall surface state. This 2D charge accumulation of a sample with area  $A$  is given by  $Q_a = gA\eta_0$ , where  $\eta_0$  is the intrinsic and quantized charge value related to the Hall conductance  $\sigma_{xy}$ , and  $g$  describes the dissipation factor related to the longitudinal conductance  $\sigma_{xx}$ . Therefore, detecting charge accumulation differs significantly from detecting  $\sigma_{xy}$  alone. While  $\sigma_{xy}$  is essentially always quantized when  $\sigma_{xx}$  is sufficiently small, the charge accumulation is generally significantly affected by the dissipation factor  $g(\sigma_{xx}/f)$ , a function of  $\sigma_{xx}/f$ . Even for small  $\sigma_{xx}$  that does not affect the detection of the quantized Hall conductance  $\sigma_{xy}$ ,  $g(\sigma_{xx}/f)$  can deviate substantially from 1. In the following paragraphs, we first describe the ideal situation of charge accumulation with no dissipation (i.e.,  $\sigma_{xx} = 0$  or  $g(\sigma_{xx}/f) = 1$ ) and derive the expression for  $\eta_0$ . We then return to the general case where  $g(\sigma_{xx}/f) \neq 1$ , providing a systematic analytical model. This general case corresponds to actual experimental conditions when working with real QAH thin film samples. Finally, an analytical expression for  $g(\sigma_{xx}/f)$  is deduced, which verifies the quantization of the intrinsic charge accumulation based on experimental data.

A clear physical picture of the intrinsic charge accumulation emerges from the Hall response of a QAH system under a time-varying magnetic field. For conceptual clarity, we illustrate this using a simple disk geometry as shown in Fig. 1a, but it is important to note that the resulting charge accumulation is a general 2D property and thus independent of the sample’s shape. When the time-varying field is applied perpendicular to the sample plane, Faraday’s law dictates that an in-plane circulating electric field is induced on both surfaces. This electric field, in turn, drives a radial Hall current on each surface due to its half-quantized Hall conductance ( $\sigma_{xy}^s = \pm e^2/2h$ ). For a single surface, the total outward current is given by:

$$I_{\text{out}} = \sigma_{xy}^s \oint_{\partial S} \mathbf{E} \cdot d\mathbf{l} = -\sigma_{xy}^s \frac{\partial \Phi}{\partial t},$$

Assuming negligible dissipation, this radial Hall current leads to a net accumulation of surface charge. Since the current flows only during the field’s variation, the resulting charge density is proportional to the change in magnetic field, given by

$$\eta_0 = \sigma_{xy} \Delta B \quad (1)$$

where  $\sigma_{xy}$  is the total Hall conductance of both surfaces combined. This model provides a direct physical link between the accumulated surface charge and the surface Hall conductance, which serves as the key observable in our experiment. Furthermore, in this ideal case without dissipation, detection of charge accumulation  $\eta_0 = \sigma_{xy}\Delta B$  can serve as a highly sensitive probe of  $\Delta B$ , i.e., essentially magnetization. This is another way of viewing the conceptual difference between the charge accumulation measurement and the Hall conductance measurement.

## 2 Experiment

### 2.1 Experimental principles and setup

In the actual experiment, a six-quintuple-layer (6-QL) chromium-doped 3D TI (Bi, Sb)<sub>2</sub>Te<sub>3</sub> (CBST) sample was prepared for the measurement, which was grown on a GaAs substrate by molecular beam epitaxy (MBE), as described in previous studies [18]. As shown in Fig. 1b, a single chip of the sample was fabricated into a device including both a Hall-bar and Corbino disk structures, each with an independent top gate. The Corbino disk structure is used for the primary measurement of field-induced charge accumulation. Its geometry with inner and outer contacts allows for the simultaneous measurement of charge pumping signals and the  $\sigma_{xx}$  via two-terminal measurements, providing crucial *in-situ* information unavailable in a simple disk-shaped sample. The Hall bar structure serves as a reference for conventional transport measurement, where the measured Hall and longitudinal resistivity ( $\rho_{yx}$  and  $\rho_{xx}$ ) relative to the magnetic field are shown in Fig. 1c, and the corresponding Hall and longitudinal conductance ( $\sigma_{xy}$  and  $\sigma_{xx}$ ) are shown in Fig. 1d. The presence of hysteresis loops with quantized  $\sigma_{xy} = \pm e^2/h$  at zero field shows a clear signature of the QAH effect. These data were measured at the temperature of approximately 200 mK with zero top gate voltage. Due to the inhomogeneity of the sample, the Fermi energy of the Corbino disk region is slightly different from that of the Hall-bar region, as concluded from the optimal gate voltages that minimize the longitudinal conductance, which are compared in Supplemental Material Fig. S1. All subsequent measurements on the Corbino disk sample were performed at its optimal gate voltage, which is defined as the voltage difference from the top gate to contact electrodes.

The 2D charge accumulation is measured via the top gate, which capacitively couples to the sample, as schematically shown in Fig. 1e. A small AC magnetic field (superimposed on the DC field) is applied perpendicular to the sample plane, which induces the target charge accumulation. The top gate is connected to a virtual ground through a current preamplifier. This configuration allows the charge accumulation in the sample to induce an image charge with opposite value on the gate, while the charge variation on the gate is probed by the current preamplifier. Therefore, the charge accumulation  $Q_a$  in the sample is transferred as a current signal  $I = 2\pi f Q_a i$ , where  $f$  is the frequency of the AC magnetic field and  $i$  represents a quadrature phase shift. The intrinsic charge accumulation signal is calculated, in turn, based on the measured current signal. In addition, a specially designed DC voltage circuit is connected to the contact electrodes, which enables DC gating of the sample while providing effective grounding in AC circuits without influencing AC signals (See Methods for details).

While the charge accumulation originates from quantized Hall conductance, it is simultaneously subject to dissipation from the sample's finite longitudinal conductance. The accumulated charge  $Q_a$  itself creates an in-plane Coulomb potential difference that drives a dissipative radial current, causing the charge to decay. The nearby grounded top gate effectively screens this potential, but a residual potential proportional to  $\eta A/C_{TG}$  (where  $\eta$  is the accumulated charge density,  $A$  is the sample area, and  $C_{TG}$  is the gate-to-sample capacitance) persists. This results in a finite decay of charge accumulation in our experiments, which modifies the ideal quantized response. However, this dissipation can be systematically characterized, allowing us to extract the intrinsic, unattenuated charge accumulation value from experimental signals, which is analyzed in subsequent sections.

### 2.2 Charge accumulation and charge pumping in QAH samples

The charge accumulation signals measured under a 277.777 Hz AC magnetic field at approximately 200 mK are presented in Fig. 2a, displaying both the in-phase (real) and quadrature (imaginary) components. All subsequent data in this paper, except for longitudinal conductivity dependence in Fig. 3c, were measured at this sample temperature. To remove background crosstalk, all signals have been anti-symmetrized

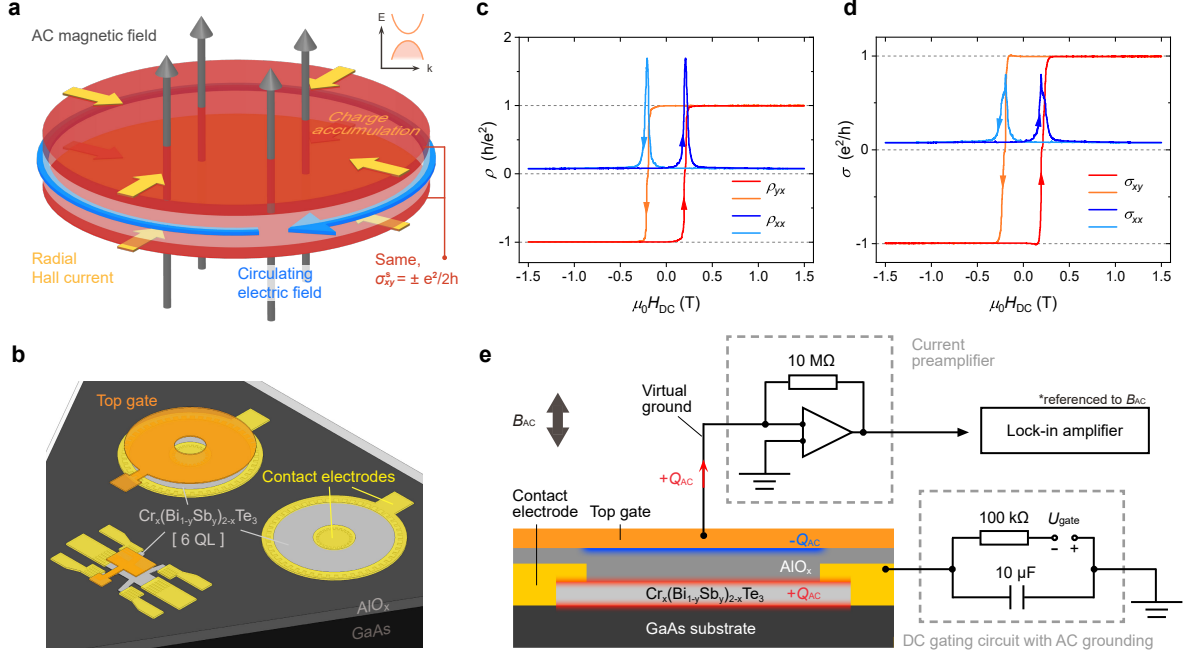


**Fig. 1 Principles of charge accumulation, basic transport of 6-QL CBST sample, and measurement configuration.** **a**, Schematic of charge accumulation in a thin-film QAH sample. The top and bottom surfaces each contribute  $\sigma_{xy}^s = \pm e^2/2h$  due to the magnetically gapped 2D surface state consisting of a massive Dirac cone. A time-varying out-of-plane field  $B_{\text{AC}}$  (vertical arrows) induces a circulating Faraday electric field (blue arrow) that drives a radial Hall current (yellow arrows) and builds surface charge (red shading) on both surfaces. **b**, Device layout including a Hall bar and two Corbino disks on a GaAs(111) substrate. The gray and yellow areas underneath the transparent  $\text{AlO}_x$  dielectric indicate the 6-QL CBST films and contact electrodes, respectively. Top gates are shown in orange. The top gate of right Corbino disk is omitted to reveal underlying structures. **c,d**, DC-field dependence of resistivity ( $\rho_{xx}, \rho_{yx}$ ) (**c**) and the corresponding conductance ( $\sigma_{xx}, \sigma_{xy}$ ) (**d**) measured on the Hall bar at  $T \approx 200$  mK and zero gate voltage. Data for upward and downward DC field sweeps are labeled with arrows. **e**, Schematic configuration of the charge accumulation measurement. A cross-section of the Corbino disk structure is displayed with the measurement circuits. Red and blue luminescence indicate the AC charge accumulation  $Q_{\text{AC}}$  in the QAH sample and the induced opposite charge  $-Q_{\text{AC}}$  under the top gate, respectively, generated by  $B_{\text{AC}}$  perpendicular to the sample plane. (The charge accumulation value  $Q_{\text{AC}}$  does not include the possible charge in the sample region beneath contact electrodes, where the charge accumulation is shielded.) The circuit on the top describes the charge measurement, where  $Q_{\text{AC}}$  is measured by a current amplifier at virtual ground and then recorded by a lock-in amplifier referenced to  $B_{\text{AC}}$ . The circuit on the right provides a DC gating voltage, while retaining the function of an effective AC short circuit due to the large parallel capacitance.

with respect to the DC magnetic field for extracting genuine signals (see Supplemental Material Section 2 for details). The data exhibit clear hysteresis loops with plateaus at high DC fields, which are consistent with the Hall conductance characteristics of the QAH effect. To facilitate comparison with the expected quantization, the total charge signal is normalized by the sample area of  $2.757 \text{ mm}^2$  (average accumulated charge density  $\eta_{\text{a}}$ ) and presented in units of  $e^2/h$  on the right vertical axis. The AC magnitude of the signal is much smaller than the quantized value, while the phase of the signal is nearly in quadrature with the AC field, which is consistent with an RC (resistance-capacitance) decaying situation as discussed before (resistance refers to  $1/\sigma_{xx}$ , and capacitance refers to  $C_{\text{TG}}$ ). Notably, while the Hall conductance ought to remain quantized near zero DC field, the charge accumulation signal decays more severely. This

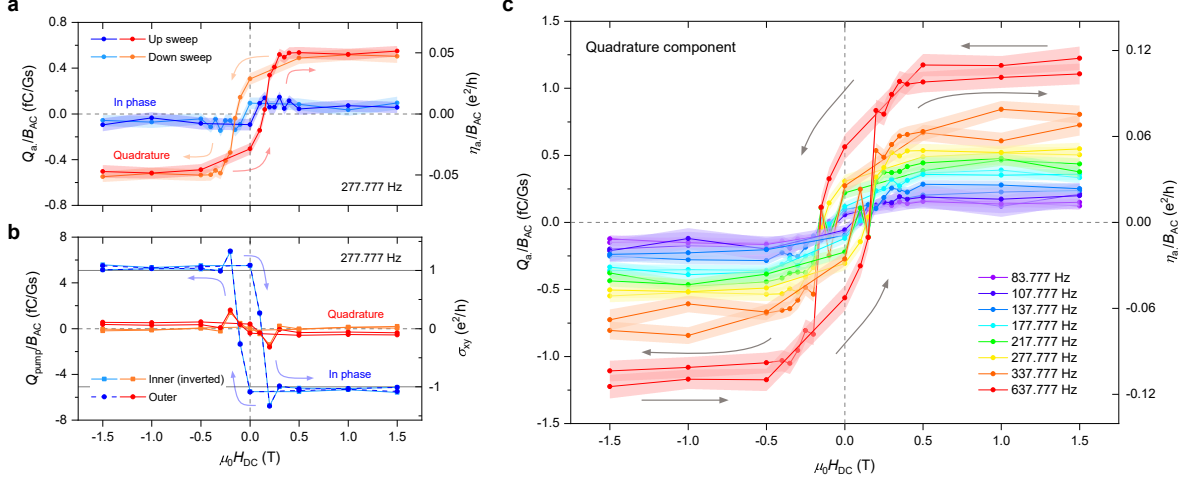


**Fig. 2 Quantized charge pumping and frequency-dependent charge accumulation in the QAH Corbino disk sample.** **a**, DC field dependence of charge accumulation at  $f = 277.777$  Hz. The left axis shows the total accumulated charge  $Q_a$ , normalized by the AC magnetic field  $B_{AC}$ , while the right axis shows the corresponding normalized charge density (spatial average)  $\eta_a/B_{AC}$  in units of  $e^2/h$ . In-phase and quadrature components are plotted separately. Shaded bands denote standard errors, which are calculated from repeated measurements. Data for upward and downward DC field sweeps are distinguished by color and labeled with arrows. **b**, DC field dependence of normalized charge pumping  $Q_{pump}/B_{AC}$  (charge flowing out of the sample) measured at  $f = 277.777$  Hz (the same conditions as in **a**). In-phase and quadrature components are displayed. Data measured at inner and outer contacts of the Corbino disk are plotted together. The inner-contact trace is inverted for direct comparison with the outer-contact trace. The arrows accompanying the in-phase data label the sweep directions of the DC field. The right axis shows the calculated Hall conductance  $\sigma_{xy}$  corresponding to the in-phase charge signal  $Q_{pump}^{in-phase}$ . **c**, Frequency dependence of the quadrature component of  $Q_a/B_{AC}$ . DC field-dependent charge accumulation measured at selected frequencies from 83.777 Hz to 637.777 Hz are shown. Axes match **a**. Upward and downward sweeps are distinguished by arrows. Shaded bands denote standard errors.

behavior is a direct consequence of the enhanced dissipation, as the longitudinal conductance increases near zero field in Fig. 1c.

For comparison, Laughlin charge pumping signals measured under the same AC field conditions are shown in Fig. 2b (see Supplemental Material Fig. S3 for detailed methods and additional data, where the idea draws on previous studies [17]). The right vertical axis in Fig. 2b represents the Hall conductance corresponding to the charge pumping signal calculated by  $\sigma_{xy} = \frac{2 \ln(r_2/r_1)}{\pi(r_2^2 - r_1^2)} \frac{Q_{pump}^{in-phase}}{B_{AC}}$  ( $r_1$  and  $r_2$  refer to the inner and outer ring radii of the Corbino disk sample), which reveals a full quantization of in-phase signals. The transition field range for the conductance reversal (0.1 T to 0.2 T) aligns perfectly with the charge accumulation data. In particular, the pumped charges at the inner and outer contacts of the Corbino disk sample show a slight difference, which reflects the charge accumulation according to charge conservation. While this difference offers an alternative way to measure charge accumulation, its precision is inevitably lower than the direct gate method (see Supplemental Material Fig. S4 for details).

Although the charge accumulation and the Laughlin charge pumping both stem from Hall conductivity ( $\sigma_{xy}$ ), they represent fundamentally different phenomena. Charge pumping describes the transport of charge across the sample and does not necessarily require the accumulation of charge. In particular, the inner and outer charge pumping signals can take (almost) the same value as described by Fig. 2b. By contrast, charge accumulation is a buildup of charge density itself on the 2D surface. This accumulated charge generates an in-plane electrostatic field  $E_r$ , which is precisely why the signal is susceptible to dissipation via  $\sigma_{xx}$  and is also what makes it a powerful probe for distinguishing the system's states, whose information cannot be obtained by simply measuring the Hall conductivity  $\sigma_{xy}$  alone.

To systematically investigate the role of dissipation, we measured charge accumulation signals across a range of frequencies, as shown in Fig. 2c. The quadrature component is plotted, as it contains the primary signal. To isolate frequency as the key variable, we adjusted the AC field amplitude at each frequency (balancing eddy current heating) to maintain a constant sample temperature, thereby keeping the longitudinal conductance fixed under the same DC field (see Supplemental Material Fig. S5 for calibration). The data in Fig. 2c shows a consistent dependence on the DC field at all frequencies, exhibiting clear plateaus at high fields. Crucially, the charge signal amplitudes increase with frequencies. This demonstrates that the detrimental effects of dissipation are mitigated at faster measurement timescales. Although the experimental setup currently limits our maximum frequency, this trend suggests that the fully quantized charge accumulation signal could eventually be reached under sufficiently suppressed decay.

### 2.3 Dissipation model and the intrinsic quantized charge accumulation

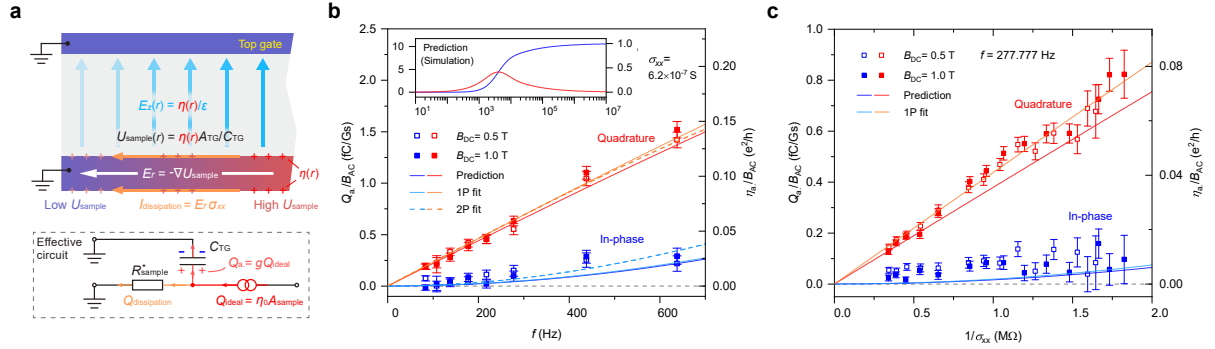


**Fig. 3 Dissipation model and quantitative fits for the field-induced charge accumulation.** **a**, Schematic of the dissipation model (top) and effective circuit (bottom). The three layers from top to bottom in the schematic are the grounded top gate, the  $\text{AlO}_x$  dielectric, and the CBST film (connected to a grounded contact at left). Vertical arrows of varying shade represent the out-of-plane electric field  $E_z$  in the dielectric, which is proportional to the charge density  $\eta$  in the sample. This out-of-plane electric field determines the potential  $U_{\text{sample}}$  in the sample and the in-plane electric field  $E_r$ , which generates the dissipative current  $I_{\text{dissipation}}$ . The effective circuit qualitatively summarizes the dissipation mechanism into three elements: a dissipative resistance  $R_{\text{sample}} \propto 1/\sigma_{xx}$ , the gate-to-sample capacitance  $C_{\text{TG}}$ , and a current source that pumps the intrinsic charge accumulation  $Q_{\text{ideal}} = \eta_0 A_{\text{sample}}$  into the sample. The measured charge accumulation is  $Q_a = g(\sigma_{xx}/f) Q_{\text{ideal}}$ . **b,c**, Frequency ( $f$ ) and longitudinal conductance ( $\sigma_{xx}$ ) dependence of the charge accumulation and parameter fits. The data are measured at fixed sample longitudinal conductance of  $6.2 \times 10^{-7}$  S (**b**) and fixed frequency of 277.777 Hz (**c**), respectively. These fixed parameters are used in the simulations and fits. The left and right vertical axes show the total accumulated charge  $Q_a$  and the corresponding average charge density  $\eta_a$ , respectively, both normalized by the AC magnetic field. In **c**, the horizontal axis is plotted as  $1/\sigma_{xx}$  for clarity. In-phase and quadrature components of the data are displayed separately. The error bars on data points manifest standard errors calculated from repeated measurements. Solid lines are the prediction of charge accumulation signals using quantized value ( $\eta_0^{(\text{unit}B)} = e^2/h$ ) and equation (3). The inset in **b** uses the same axes as **b** and shows an extended frequency range of the prediction, illustrating the crossover from dissipation-dominated to near-ideal charge accumulation. Light solid lines are one-parameter fits of equation (3) with free  $\eta_0^{(\text{unit}B)}$ . Light dashed lines in **b** are two-parameter fits of equation (3) with free  $\eta_0^{(\text{unit}B)}$  and dissipation parameter  $\lambda_f = \frac{\sigma_{xx} A_{\text{TG}}}{C_{\text{TG}}}$ .

Since dissipation modifies the quantized signal, we employ a quantitative model to extract the intrinsic, undissipated value of the charge accumulation. A conceptual schematic of this model is shown in



Fig. 3a. The charge accumulation density  $\eta$  determines the potential  $U_{\text{sample}}$  in the Corbino disk sample, which generates the dissipation current  $I_{\text{dissipation}}$  and alters the value of the accumulated charge. A qualitative circuit is displayed below the schematic, where the microscopic dissipation mechanism is simplified as an effective resistance  $R_{\text{sample}}$ . The dissipative charge  $Q_{\text{dissipation}}$  flowing through this resistance divides the ideal charge accumulation  $Q_{\text{ideal}} = \eta_0 A_{\text{sample}}$ , leaving a real accumulated charge as  $Q_{\text{a.}} = gQ_{\text{ideal}}$  in the sample. In a quantitative model, three factors govern the dissipation: the gate-to-sample capacitance ( $C_{\text{TG}}$ ), which sets the potential rise generated per unit of accumulated charge; the longitudinal conductance ( $\sigma_{xx}$ ), which determines the dissipative current generated by the potential rise; and the AC frequency ( $f$ ), which dictates the timescale for the decay. As derived in the Supplemental Material Section 6, the physical picture of charge accumulation with dissipation is captured by a differential equation for the complex charge density,  $\tilde{\eta}$  (the complex number corresponds to the phase information of the AC signal):

$$(1 + i \frac{\sigma_{xx} A_{\text{TG}}}{2\pi f C_{\text{TG}}} \nabla^2) \tilde{\eta} = \sigma_{xy} B_{\text{AC}} = \eta_0^{(\text{unit}B)} B_{\text{AC}} \quad (2)$$

where  $A_{\text{TG}}$  is the top gate area (note that  $A_{\text{TG}}$  is slightly larger than the sample area because the top gate also covers part of contact electrodes). The analytical solution to this equation for our Corbino disk geometry (with inner ring radius of  $r_1$  and outer ring radius of  $r_2$ ) provides a testable model, which corresponds to a total accumulated charge  $\tilde{Q}_{\text{a.}}$  as

$$\tilde{Q}_{\text{a.}}/B_{\text{AC}} = \int_{r_1}^{r_2} 2\pi r dr \tilde{\eta}(r) = g(\sigma_{xx}/f) \pi(r_2^2 - r_1^2) \eta_0^{(\text{unit}B)} \quad (3)$$

where  $\pi(r_2^2 - r_1^2)$  is the area of the Corbino disk sample, and  $g(\sigma_{xx}/f)$  is the dissipation factor discussed previously. Its detailed expression is

$$g(\sigma_{xx}/f) = \left\{ 1 + \frac{2}{k(r_2^2 - r_1^2) (J_0(kr_1)Y_0(kr_2) - J_0(kr_2)Y_0(kr_1))} \times \right. \\ \left. [(Y_0(kr_1) - Y_0(kr_2)) \cdot (r_2 J_1(kr_2) - r_1 J_1(kr_1)) + \right. \\ \left. (J_0(kr_2) - J_0(kr_1)) \cdot (r_2 Y_1(kr_2) - r_1 Y_1(kr_1))] \right\} \quad (4)$$

$$\text{where} \quad k(\sigma_{xx}/f) \equiv \sqrt{\frac{2\pi C_{\text{TG}} f}{i A_{\text{TG}} \sigma_{xx}}} \quad (5)$$

(Detailed calculation is placed in Supplemental Material Section 6). To validate this model and extract the quantization, we performed two independent experiments, measuring the charge accumulation as a function of frequency ( $f$ ) and then as a function of longitudinal conductance ( $\sigma_{xx}$ ). The theoretical solution (equation (3)) is fitted to these two datasets, with the intrinsic charge accumulation density (per unit AC field)  $\eta_0^{(\text{unit}B)} = \eta_0/B_{\text{AC}}$  serving as the primary fitting parameter, whose theoretical value is  $e^2/h$ . The geometric parameters of the Corbino disk ( $r_1 = 350 \text{ } \mu\text{m}$ ,  $r_2 = 1000 \text{ } \mu\text{m}$ ) are treated as known constants throughout the analysis.

We first measured and analyzed the frequency dependence of charge accumulation, with the results shown in Fig. 3b. To isolate frequency as the variable, we kept the longitudinal conductance stable around  $\sigma_{xx} = 6.2 \times 10^{-7} \text{ S}$  by adjusting the AC field amplitude at each frequency to maintain a stable sample temperature. Experimental data (scatter points with error bars displaying the standard error) were measured at DC fields of  $\pm 0.5 \text{ T}$  and  $\pm 1.0 \text{ T}$ . These fields were specifically chosen because they lie deeply within the QAH plateau, where  $\sigma_{xx}$  is small and stable, ensuring reliable experimental conditions. The data from both fields are identical within experimental error, confirming the signal's stability. Before performing the fitting, we first compared the data to a theoretical prediction (solid lines). It was calculated using the expected quantized value  $\eta_0^{(\text{unit}B)} = e^2/h$  combined with independently measured parameters for  $C_{\text{TG}}$  (2.00 nF, see Supplemental Material Fig. S7 for the measurement method) and  $\sigma_{xx}$  ( $6.2 \times 10^{-7} \text{ S}$ ). Experimental data show agreement with the prediction within error, providing initial validation of

our model. Furthermore, as highlighted by the inset, our measurements lie within the severe decay region, where the model correctly predicts the observed linear dependence of the quadrature component on frequency.

**Table 1** Fitting results for the intrinsic charge accumulation. The uncertainty represents the 95% confidence interval.

Experiment	Parameter	Fitted Value	Theoretical Value
<i>A. Frequency Dependence</i>			
1-Parameter Fit <sup>a</sup>	$\eta_0^{(\text{unit}B)} (e^2/h)$	$1.05 \pm 0.06$	1
2-Parameter Fit	$\eta_0^{(\text{unit}B)} (e^2/h)$	$0.69 \pm 0.20$	1
	$\lambda_f (10^{-3} \text{ m}^2/\text{s})$	$0.71 \pm 0.20$	$1.09^b$
<i>B. <math>\sigma_{xx}</math> Dependence</i>			
1-Parameter Fit <sup>c</sup>	$\eta_0^{(\text{unit}B)} (e^2/h)$	$1.16 \pm 0.06$	1

<sup>a</sup>Independently measured values are used:  $\sigma_{xx} = 6.2 \times 10^{-7} \text{ S}$ ,  $A_{\text{TG}} = 3.52 \times 10^{-6} \text{ m}^2$ , and  $C_{\text{TG}} = 2.00 \text{ nF}$ .

<sup>b</sup>Theoretical value of  $\lambda_f = \sigma_{xx} A_{\text{TG}} / C_{\text{TG}}$  is calculated from independently measured values represented above<sup>a</sup>.

<sup>c</sup>Independently measured values are used:  $f = 277.777 \text{ Hz}$ ,  $A_{\text{TG}} = 3.52 \times 10^{-6} \text{ m}^2$ , and  $C_{\text{TG}} = 2.00 \text{ nF}$ .

To quantitatively extract the intrinsic signal  $\eta_0^{(\text{unit}B)}$ , we then fit the model (equation (3)) to the data, with the results summarized in Table 1. Our primary approach is a constrained, one-parameter fit (light solid lines), where the dissipation parameters  $C_{\text{TG}}$  and  $\sigma_{xx}$  were fixed to their independently measured values, leaving only  $\eta_0^{(\text{unit}B)}$  as a free parameter. This fit was successful, yielding an  $\eta_0^{(\text{unit}B)}$  value consistent with the quantized value of  $e^2/h$  with only a 5% deviation. For comparison, we also performed a two-parameter fit (light dashed lines) where the dissipation term  $\lambda_f = \frac{\sigma_{xx} A_{\text{TG}}}{C_{\text{TG}}}$  was treated as a second free parameter. However, because the main data lie in a nearly linear regime, this less-constrained fit lacks the sensitivity to reliably separate the contributions from  $\eta_0^{(\text{unit}B)}$  and dissipation. This limitation highlights the importance of using accurately determined dissipation parameters. The success of the one-parameter fit, which relies on these independently measured values, therefore provides quantitative evidence that the intrinsic charge accumulation is indeed quantized at  $e^2/h$ .

As a second, independent validation of the model, we analyze the charge accumulation's dependence on longitudinal conductance, with the results shown in Fig. 3c. The experiment was performed at a fixed frequency of 277.777 Hz, while  $\sigma_{xx}$  was tuned by varying the AC field amplitude, which controls the sample temperature via eddy current heating.  $\sigma_{xy}$  was confirmed to remain quantized across the entire temperature range by simultaneously monitoring the Hall-bar sample. The charge accumulation signals, measured at DC fields of  $\pm 0.5 \text{ T}$  and  $\pm 1.0 \text{ T}$ , are plotted (scatter points) against  $1/\sigma_{xx}$ , which plays a role analogous to frequency in the decay model. The data are compared with a theoretical prediction (solid lines), which is calculated using the expected quantized value  $\eta_0^{(\text{unit}B)} = e^2/h$  and independently measured parameters ( $C_{\text{TG}} = 2.00 \text{ nF}$ ,  $f = 277.777 \text{ Hz}$ ). The experimental data show agreement with this prediction, further validating the model. To quantitatively extract the intrinsic signal, we again employ the one-parameter fitting on equation (3), leaving only  $\eta_0^{(\text{unit}B)}$  as the free parameter. The resulting fit (light solid lines), as detailed in Table 1, yields an intrinsic charge accumulation of  $\eta_0^{(\text{unit}B)} = 1.16 \pm 0.06 e^2/h$ . This value is also in agreement with the theoretical quantum of  $e^2/h$ . The success of this one-parameter fit, performed on an independent data set, provides powerful, corroborating evidence that the underlying charge accumulation is indeed quantized.

### 3 Discussion

The topological magnetoelectric effect (TME) in three-dimensional topological insulators (3D TIs) is a condensed matter manifestation of the four-dimensional quantum Hall (4D QH) effect [19, 8, 20]. The TME is characterized by the relationship  $\Delta P = \frac{e^2}{2h} N_{\text{Ch}}^{(2)} \Delta B$ , where  $N_{\text{Ch}}^{(2)}$  is the second Chern number (an integer), and the four-dimensional parameter space combines three spatial dimensions with time. Our observation of field-induced quantized charge accumulation in the quantum anomalous Hall (QAH)



state [4–7] of a 3D TI stems from two-dimensional (2D) quantum Hall (QH) physics originating in the 2D surface state, distinct from the 4D QH physics. However, our findings are deeply connected to 4D QH physics, both technologically and fundamentally. The TME emerges in a 3D TI when its surface magnetizations are oriented all inward or all outward, creating an axion insulator (AI) state [21–27]. In this state, a magnetic field difference ( $\Delta B$ ) induces a quantized parallel electric polarization difference ( $\Delta P$ ) in the bulk, governed by the coefficient  $\frac{e^2}{2h} N_{\text{Ch}}^{(2)}$ . In a thin AI film with a perpendicular magnetic field, this polarization difference manifests as quantized surface charge accumulation of opposite signs:  $\frac{e^2}{2h} \Delta B$  on one surface and  $-\frac{e^2}{2h} \Delta B$  on the other (the signs reverse if the sign of  $N_{\text{Ch}}^{(2)}$  changes). In contrast, the QAH state of a 3D TI, unlike the single-domain 4D QH state of the AI, forms multi-domain states with  $N_{\text{Ch}}^{(2)} = \pm 1$ , which cancels the total bulk electric polarization difference. This results in quantized surface charge accumulation of the same sign  $\frac{e^2}{2h} \Delta B$  or  $-\frac{e^2}{2h} \Delta B$  on both surfaces (as a result  $\frac{e^2}{h} \Delta B$  or  $-\frac{e^2}{h} \Delta B$  for the total charge accumulation), consistent with parallel magnetization directions on both surfaces. Both QAH and AI states exhibit quantized charge accumulation on a single surface. However, in the QAH state, bulk 4D QH signals cancel, leaving only the 2D quantized charge accumulation characteristic of 2D QH physics. In the AI state, the 4D QH signals persist, manifesting as a quantized electric polarization difference, observable as oppositely signed charge accumulation on the top and bottom surfaces. Because the TME’s experimental signature is also surface charge (with opposite signs), our methodology provides a direct path to its detection. We have demonstrated sensitive surface charge accumulation measurement and quantitative modeling to overcome inherent dissipation effects. While our single-gate geometry detects the net charge accumulation of the QAH state (2D QH), detecting the TME’s quantized electric polarization difference (4D QH) requires a dual-gate structure to measure the potential difference between the top and bottom surfaces. This presents a significant experimental challenge but builds upon the same fundamental principles that we have validated. Our work thus offers a promising pathway towards directly detecting the TME’s quantized electric polarization difference and exploring the 4D QH effect in condensed matter physics.

## 4 Methods

### 4.1 Thin-film growth and device fabrication

The device including the Corbino disk and Hall bar geometries was fabricated from a 6-QL CBST film grown by molecular beam epitaxy (MBE) on a GaAs substrate. To minimize sample degradation, all patterning steps were performed using Molybdenum (Mo) shadow masks in a solvent-free process. First, the film was patterned via argon ion milling to define the device mesa. Subsequently, Ti/Au (3 nm/47 nm) contact electrodes were deposited by thermal evaporation. The inner and outer radii of the Corbino disk sample’s contact electrodes are 350  $\mu\text{m}$  and 1000  $\mu\text{m}$ , respectively, corresponding to a sample area of 2.757  $\text{mm}^2$ . A 140 nm thick  $\text{AlO}_x$  gate dielectric was then deposited at room temperature using oxygen plasma-assisted atomic layer deposition (ALD). Finally, Ti/Au (8 nm/72 nm) top gates were evaporated. For the Corbino disk sample, the top gate partially overlaps the area of the contact electrodes (90  $\mu\text{m}$  width) to fully cover the entire sample, which has a total area of 3.520  $\text{mm}^2$ . The insulation of the large-area top gate was ensured by the thick  $\text{AlO}_x$  dielectric and a smooth topography at edges of contact electrodes. This smooth topography, which mitigates defects in the overlying dielectric, is the result of the shadow mask method coupled with sample rotation during metal evaporation.

### 4.2 In-plane transport measurement

The Hall resistance ( $\rho_{yx}$ ) and longitudinal resistance ( $\rho_{xx}$ ) of the Hall-bar sample were measured using a standard low-frequency AC lock-in technique. An excitation current of 10 nA (13.777 Hz) was applied to the sample, calibrated via a 100 k $\Omega$  series resistor. The resulting transverse and longitudinal voltages were detected using lock-in amplifiers (Stanford Research Systems, models SR830 and SR865A). The Hall conductance ( $\sigma_{xy}$ ) and longitudinal conductance ( $\sigma_{xx}$ ) were then obtained by inverting the resistivity tensor.

For the Corbino disk sample, the longitudinal conductance was determined using a two-terminal, constant-voltage method. A 5  $\mu\text{V}$  AC (13.777 Hz) voltage ( $U_c$ ) was applied between the inner and outer

contacts, and the resulting current ( $I_c$ ) was measured with a custom-built transimpedance current preamplifier ( $10^7$  V/A gain, based on an ADA4530-1 chip) connected to a lock-in amplifier (model SR830). The conductance was calculated using the standard Corbino formula:  $\sigma_{xx} = \frac{\ln(r_2/r_1)}{2\pi} I_c / U_c$ , where  $r_1$  and  $r_2$  are the radii of the inner and outer contacts, respectively.

### 4.3 AC magnetic field generation

The AC magnetic field was generated by two identical small coils arranged to clamp the sample holder. The entire coil assembly was anchored to the cold finger of 1 K still plate in the dilution refrigerator, which ensures the same center between the AC field and the DC field, and their perpendicularity to the sample plane. Each coil was constructed by winding a 0.438 mm diameter Cu-clad NbTi superconducting wire onto a brass bobbin. The solenoid has a total of approximately 340 turns, with an inner diameter of 24 mm and a length of 15 mm. The two coils were mounted coaxially with a separation of 11 mm to form a Helmholtz pair, ensuring high field homogeneity near the sample. To shield against capacitive coupling, each coil was wrapped with a 0.2 mm thick copper foil (as a Faraday cage). The two coils were wired in series, and this pair was driven by the differential sine outputs of an SR865A lock-in amplifier (50  $\Omega$  output impedance per terminal), providing a zero-mean-voltage excitation to minimize measurement crosstalk.

The amplitude and phase of the resulting AC magnetic field were calibrated in-situ at each measurement frequency in a static DC field of 0.01 T. The calibration was performed using a Hall sensor fabricated from a GaAs/AlGaAs heterostructure containing a 2D electron gas. For the calibration, a 1  $\mu$ A DC current was applied to pass through the sensor, and the resulting AC Hall voltage was measured with a lock-in amplifier. The AC field was then determined by comparing this AC voltage to the sensor's calibrated DC Hall coefficient ( $k_{\text{Hall}} = \Delta\rho_{yx}/\Delta B$ ). To remove background crosstalk in the AC voltage, this process was repeated with a reversed DC current (-1  $\mu$ A) and the results were anti-symmetrized. The complete, calibrated AC field response per volt of excitation is presented in Supplemental Material Fig. S8. In order to maintain a low and constant sample temperature, we used small and frequency-dependent AC field amplitudes, as shown in Supplemental Material Fig. S5. The range of AC field amplitude in the experiment was 0.033 Gs to 0.180 Gs (637.777 Hz to 83.777 Hz, RMS value).

### 4.4 Charge signal measurement

The charge accumulation induced by the AC magnetic field was measured on the Corbino disk sample (Fig. 1b,e). The resulting AC signal was detected as a current from the top gate, which was connected to the virtual ground input of a custom-built current preamplifier ( $10^7$  V/A gain, based on an ADA4530-1). This configuration ensures the measured current corresponds directly to the charge variation within the sample. The amplifier's output was measured by a lock-in amplifier, referenced to the AC field's source (an SR865A). The preamplifier was located at room temperature and connected to the sample's top gate via a low-resistance coaxial cable. Because the amplifier's virtual ground holds the cable's core conductor at the same potential as its grounded shield, the parasitic capacitance of the cable (about 900 pF, same magnitude as the  $C_{\text{TG}}$  of the sample) has a negligible effect on the measurement.

A DC gate voltage was applied to tune the sample's Fermi level (Fig. 1e). The optimal gate potential of +9.4 V (gate relative to sample) was identified as the point of minimum longitudinal conductance. To isolate the DC gating circuit from the AC measurement, a bias voltage was applied to the sample's contacts while the gate remained at ground potential. Specifically, both Corbino contacts were biased to -9.4 V using a National Instruments PXIe-4322 module, with a 100 k $\Omega$  series resistor for current protection. To provide a low-impedance path for AC currents, a 10  $\mu$ F bypass capacitor was connected between the sample contacts and ground. This capacitor effectively shorts the gating circuit at the measurement frequencies (e.g., presenting impedance of only 190  $\Omega$  at 83.777 Hz) while maintaining the desired DC potential on the sample.

Since the charge accumulation is sensitive to the longitudinal conductance and corresponding temperature, we measured signals at several DC field points rather than continuously sweeping the field, which would generate extra temperature variation. Each point was held for 900 seconds to ensure a stable temperature, and the data from the last 300 seconds were recorded.

## 5 Acknowledgements

T.L. acknowledges the support for the project by the National Key Research and Development Program of China (No. 2021YFA1401600). Y.Liu acknowledges the support by the National Key Research and Development Program of China (Grant No. 2021YFA1401900). We thank Xing He and Wanjun Jiang for providing access to their Ar ion etching system, which was used for sample fabrication. We also thank Daiqiang Huang for his discussions with us on the cryogenic coil structure. Y.Li thanks Lewei Li for her help with the schematic preparation.

## 6 Author contribution

T.L. conceived and designed the project, provided overall direction, supervised the experiments, and coordinated collaborations among the research groups. Y.Li and J.C. designed the ultrahigh-sensitivity experimental setup for charge accumulation detection and performed the measurements with extensive assistance from R.W. and Y.Liu, as well as through in-depth discussions with T.L. R.W. and Y.Liu developed the custom ultrahigh-sensitivity current preamplifier. The high-quality quantum anomalous Hall thin films were grown by Y.Z. and X.K. and subsequently characterized and fabricated by Y.Li with support from J.C., Y.D., and J.X. Analyses of measurements were conducted by Y.Li and T.L. The manuscript was written by Y.Li and T.L. with input from all authors. All authors discussed the results and provided feedback for the manuscript.

## 7 Competing interests

The authors declare no competing interests.

## References

- [1] Yu, R. *et al.* Quantized anomalous Hall effect in magnetic topological insulators. *Science* **329**, 61–64 (2010).
- [2] Hasan, M. Z. & Kane, C. L. Colloquium: Topological insulators. *Rev. Mod. Phys.* **82**, 3045–3067 (2010).
- [3] Qi, X.-L. & Zhang, S.-C. Topological insulators and superconductors. *Rev. Mod. Phys.* **83**, 1057–1110 (2011).
- [4] Chang, C.-Z. *et al.* Experimental observation of the quantum anomalous Hall effect in a magnetic topological insulator. *Science* **340**, 167–170 (2013).
- [5] Kou, X. *et al.* Scale-invariant quantum anomalous Hall effect in magnetic topological insulators beyond the two-dimensional limit. *Phys. Rev. Lett.* **113**, 137201 (2014).
- [6] Checkelsky, J. G. *et al.* Trajectory of the anomalous Hall effect towards the quantized state in a ferromagnetic topological insulator. *Nature Phys.* **10**, 731–736 (2014).
- [7] Deng, Y. *et al.* Quantum anomalous Hall effect in intrinsic magnetic topological insulator MnBi<sub>2</sub>Te<sub>4</sub>. *Science* **367**, 895–900 (2020).
- [8] Qi, X.-L., Hughes, T. L. & Zhang, S.-C. Topological field theory of time-reversal invariant insulators. *Phys. Rev. B* **78**, 195424 (2008).
- [9] Morimoto, T., Furusaki, A. & Nagaosa, N. Topological magnetoelectric effects in thin films of topological insulators. *Phys. Rev. B* **92**, 085113 (2015).

- [10] Zhang, F., Kane, C. L. & Mele, E. J. Surface state magnetization and chiral edge states on topological insulators. *Phys. Rev. Lett.* **110**, 046404 (2013).
- [11] Wu, L. *et al.* Quantized Faraday and Kerr rotation and axion electrodynamics of a 3D topological insulator. *Science* **354**, 1124–1127 (2016).
- [12] Okada, K. N. *et al.* Terahertz spectroscopy on Faraday and Kerr rotations in a quantum anomalous Hall state. *Nat. Commun.* **7**, 12245 (2016).
- [13] Ikebe, Y. *et al.* Optical Hall effect in the integer quantum Hall regime. *Phys. Rev. Lett.* **104**, 256802 (2010).
- [14] Shimano, R. *et al.* Quantum Faraday and Kerr rotations in graphene. *Nat. Commun.* **4**, 1841 (2013).
- [15] Laughlin, R. B. Quantized Hall conductivity in two dimensions. *Phys. Rev. B* **23**, 5632–5632 (1981).
- [16] Dolgoplov, V. T., Shashkin, A. A., Zhitenev, N. B., Dorozhkin, S. I. & Von Klitzing, K. Quantum Hall effect in the absence of edge currents. *Phys. Rev. B* **46**, 12560–12560 (1992).
- [17] Kawamura, M. *et al.* Laughlin charge pumping in a quantum anomalous Hall insulator. *Nature Phys.* **19**, 333–337 (2023).
- [18] Ji, Y. *et al.* Thickness-driven quantum anomalous Hall phase transition in magnetic topological insulator thin films. *ACS Nano* **16**, 1134–1141 (2022).
- [19] Zhang, S.-C. & Hu, J. A four-dimensional generalization of the quantum Hall effect. *Science* **294**, 823–828 (2001).
- [20] Essin, A. M., Moore, J. E. & Vanderbilt, D. Magnetoelectric polarizability and axion electrodynamics in crystalline insulators. *Phys. Rev. Lett.* **102**, 146805 (2009).
- [21] Mogi, M. *et al.* A magnetic heterostructure of topological insulators as a candidate for an axion insulator. *Nat. Mater.* **16**, 516–521 (2017).
- [22] Mogi, M. *et al.* Tailoring tricolor structure of magnetic topological insulator for robust axion insulator. *Sci. Adv.* **3**, eaao1669 (2017).
- [23] Xiao, D. *et al.* Realization of the axion insulator state in quantum anomalous Hall sandwich heterostructures. *Phys. Rev. Lett.* **120**, 056801 (2018).
- [24] Liu, C. *et al.* Robust axion insulator and Chern insulator phases in a two-dimensional antiferromagnetic topological insulator. *Nat. Mater.* **19**, 522–527 (2020).
- [25] Xu, Y. *et al.* Observation of topological surface state quantum Hall effect in an intrinsic three-dimensional topological insulator. *Nature Phys.* **10**, 956–963 (2014).
- [26] Zhuo, D. *et al.* Axion insulator state in hundred-nanometer-thick magnetic topological insulator sandwich heterostructures. *Nat. Commun.* **14**, 7596 (2023).
- [27] Bai, Y. *et al.* Quantized anomalous Hall resistivity achieved in molecular beam epitaxy-grown MnBi<sub>2</sub>Te<sub>4</sub> thin films. *Natl. Sci. Rev.* **11**, nwad189 (2024).